Impact of ionization potential depression on single particle imaging

Sourav Banerjee [1,*] Zoltan Jurek [1,2] Rui Jin [3] Sang-Kil Son [1] and Robin Santra [1,2,4]

[1]*Center for Free-Electron Laser Science CFEL, Deutsches Elektronen-Synchrotron DESY, Notkestraße 85, 22607 Hamburg, Germany*

[2]*The Hamburg Centre for Ultrafast Imaging, Luruper Chaussee 149, 22761 Hamburg, Germany*

[3]*National Key Laboratory of Computational Physics, Institute of Applied Physics and Computational Mathematics, Beijing 100088, China*

[4]*Department of Physics, University of Hamburg, Notkestraße 9–11, 22607 Hamburg, Germany*

(Received 8 July 2025; accepted 12 December 2025; published 13 January 2026)

Ultraintense and ultrashort x-ray free-electron laser (XFEL) pulses promise single particle imaging (SPI) via enabling collection of diffraction data for nanocrystals, or nano-size nonperiodic objects before the destruction of the sample. Photoionization and subsequent processes lead to plasma generation within the sample in such experiments. The continuum energy levels of electrons for atoms and atomic ions are lowered due to plasma screening, also known as ionization potential depression (IPD). We theoretically investigate the plasma formation and the effect of IPD in the context of SPI with calculations performed on bulk glycine, mimicking the interior of irradiated biological macromolecules, e.g., proteins or viruses. To simulate the plasma formation dynamics, we employ a nonequilibrium, hybrid quantum-classical approach, combined with the evaluation of the transient IPD from first-principles electronic structure calculations considering the time-dependent microscopic environment, which in earlier work was applied to a solid-density plasma consisting of a single atomic species [Phys. Rev. E **106**, 015206 (2022)]. Here, this approach is extended to more than one atomic species for applications to biological macromolecules in SPI studies. Our work quantifies the effect and importance of IPD in XFEL-based imaging of biological systems and provides further guidance for simulations of electronic radiation damage dynamics toward successful SPI experiments.

DOI: 10.1103/6vbz-cxkn

I. INTRODUCTION

One of the most important questions in the present age of molecular biology is the determination of protein structures and understanding their function as they form the basis of life [1]. Traditional x-ray crystallography has been an efficient and successful technique to determine structures for a large number of proteins [2]; however, the bottleneck lies in the fact that many protein macromolecules, especially membrane proteins, are difficult to crystallize [3]. Moreover, a recent breakthrough in predicting protein structures from available amino-acid sequence data has been made using AlphaFold [4–8], but it still has limitations, for example, considering protein-protein interactions and multiple conformations in a limited way [9]. Cryogenic electron microscopy as well has made remarkable progress [10–12] in achieving near-atomic resolution for static structures. Even with all these developments, the challenge is still capturing conformational changes or transient states of a single biomolecule within a near-physiological environment at room temperature.

The high-intensity and ultrashort pulses generated by x-ray free-electron laser (XFEL) sources open the arena for such single particle imaging (SPI) studies [13–15]. XFELs have proven successful not only in determining structures of nanocrystals with serial femtosecond crystallography (SFX) [16–21] and carrying out time-resolved SFX studies [22–24], but also in imaging living cells [25], cell organelles [26], and viruses [27–30]. Due to the ultrashort pulse duration, atomic motions in the sample are effectively frozen, so that measurements can be performed at physiological temperatures (particularly if measured in a liquid environment) [31]. A significant number of works [32–38] within the past few years have been pushing the field of SPI because of its importance; yet, atomic resolution SPI has not been reached.

XFEL sources are capable to deliver pulses with a few-femtosecond temporal duration, having a photon energy in the hard x-ray regime, which is desirable for high-resolution SPI experiments. Though the concept of "diffraction before destruction" underlies this approach to molecular structure determination, radiation damage is nonetheless a limiting factor in such studies [39,40]. X-ray photons from XFEL pulses participate in photoionizing an organic sample that is exposed to it, at a much higher rate than in elastic scattering. Photoelectrons and subsequently generated Auger-Meitner electrons further enhance ionization of the atoms via collisions, leading to a severe modification of the electronic structure of the sample. Thus, high-intensity XFEL pulses inevitably turn the irradiated region of the sample into a plasma.

Both theoretical and experimental studies exist on XFEL-induced plasma formation in solids [41,42] and in nano-size atomic clusters [43–45]. Also, theoretical studies of plasma formation in protein crystals [23,40,46,47] have been

*Contact author: sourav.banerjee@desy.de

performed. Within plasmas, the threshold energy required to further ionize an atomic ion is lowered compared to the scenario where atomic ions are isolated, because of the screening by the plasma environment. This phenomenon is known as ionization potential depression (IPD) [48,49]. It has been widely discussed in the context of solid-density plasmas [41,50–55], but it has been mostly omitted in simulations of plasmas formed in biological molecules in the context of SPI, with a few exceptions [56,57]. To the best of our knowledge, no IPD measurements on biological macromolecules, x-ray-heated to SPI-relevant conditions, exist.

It is important to note that XFEL-generated plasma lies far from local thermodynamic equilibrium (LTE) [58] within the XFEL pulse duration. This is because (1) the electron-ion relaxation timescale is picoseconds [59,60], i.e., orders of magnitude longer than the duration of such XFEL pulses, and (2) even the electron-electron relaxation time is typically a few tens to hundreds of femtoseconds (in case of biological systems irradiated by hard x-rays) [61–63], which is comparable to the XFEL pulse duration. Hence, non-LTE (NLTE) or nonequilibrium approaches are, in general, critical for describing XFEL-created plasmas [64]. Such plasmas have been treated not only with an LTE approach based on the two-temperature method [65–67], but also with various NLTE approaches [68–72] where detailed atomic dynamics are considered based on collisional-radiative models [64,73]. Available NLTE plasma codes such as CRETIN [68] and FLYCHK [69] still evaluate IPD within LTE conditions, e.g., using the Ecker-Kröll [48] or Stewart-Pyatt [49] model.

In the present study, we address the impact of IPD on electronic radiation damage of biological macromolecules under realistic irradiation conditions, using a nonequilibrium approach. To this end, we employ XMDYN, a Monte Carlo- and molecular-dynamics (MC-MD)-based simulation tool [74,75] to describe the nonlocality and nonthermal-equilibrium features of XFEL-produced plasmas [76–80].

II. METHODOLOGY

Here, we provide a brief review of the MC-MD approach implemented in XMDYN [75,81], which is used in the present work. Detailed implementations can be found in Ref. [74]. XMDYN is a modeling framework that provides a microscopic description of the dynamics of matter exposed to intense x-ray pulses. By utilizing an approximate first-principles (hybrid quantum-classical) description of the elementary processes and of the interactions between particles, XMDYN evolves the particles in time, without imposing any assumptions about thermodynamic/statistical properties of the system. One simulation run yields a realization of the stochastic dynamics (later referred to as a trajectory), i.e., a time series of snapshots containing particle properties (position, velocity, charge, electronic configuration, etc.) of the evolving system perturbed by the stochastic ionization events. In the XMDYN framework, neutral atoms, atomic ions, and free electrons are treated as classical particles; i.e., their motion in real space is governed by Newton's equations of motion. The dynamics of electron configurations of atoms and atomic ions are described by tracking the occupation numbers of individual atomic orbitals via a Monte Carlo on-the-fly algorithm. The atomic electronic structures are obtained by using XATOM [74,81,82], which performs *ab initio* [Hartree-Fock-Slater (HFS)] quantum-mechanical calculations for individual electron configurations formed during the dynamics, providing atomic parameters such as orbital binding energies of atoms and atomic ions, as well as cross sections and rates for relevant x-ray-induced physical processes (photoionization, Auger-Meitner decay, and fluorescence). Collisional ionization and recombination are handled with semiclassical algorithms in XMDYN, relying on the computed orbital energies.

To incorporate the plasma environment effects into the atomic electronic structure, we utilize real-time and real-space information of atomic ions and free electrons from individual XMDYN simulations [79]. At every time point, the atomic environmental potentials V_A^{env} are constructed for a given atomic particle A with the positions of ions and electrons after spherical averaging, and then they are grouped into individual charge states of a single atomic species and further averaged over all atomic particles in the respective charge states. The transient IPD effects of an atom are then captured by taking the constructed plasma environmental potential into consideration as an external potential within the self-consistent-field (SCF) scheme of HFS. By choosing whether or not we incorporate the plasma environmental potential into the atomic electronic structure calculation, we perform XMDYN simulations with or without IPD feedback. This framework has been tested for dense aluminum plasmas [79], where it quantitatively reproduced the atomic ionization potential shifts caused by the IPD effect in comparison with experiment [41]. Also, it has been demonstrated that the IPD effects are important in theoretical modeling of nonequilibrium evolution of aluminum dense plasmas [80].

For the present study of biological molecules, the modeling framework has been extended to treat systems consisting of more than one atomic species. We group the atoms and atomic ions into classes according to their element type and charge state (i.e., classes of C^{1+}, C^{2+}, N^{2+}, O^{2+}, etc.). At every time point during an XMDYN simulation, each atomic particle finds itself in a different local environment; i.e., it experiences a different plasma environmental potential V_A^{env}. For the sake of numerical efficiency, we assign to each class at a given time point a single plasma environmental potential (i.e., $V_{\text{class}}^{\text{env}}$) by averaging the individual environmental potentials over all atomic particles in that class, which can be expressed as

$$V_{\text{class}}^{\text{env}}(r) = \frac{1}{N_{\text{class}}} \sum_{A}^{\text{class}} V_A^{\text{env}}(r),$$

where N_{class} is the number of atomic particles in the given class. Note that the influence of this averaging scheme was discussed in Ref. [79]. In addition to the spherical averaging (required for a central atomic potential) and the environmental potential averaging schemes, a soft-core potential [74,79] is employed to avoid the Coulomb singularity. Those treatments tend to reduce the sensitivity to transient local structures in the IPD calculations.

For every atomic configuration in the corresponding electronic structure calculations, the environment potential of the class is used to which the given configuration belongs. For example, electronic energy levels for the O^{1+} configurations

$1s^2 2s^2 2p^3$, $1s^2 2s^1 2p^4$, and $1s^1 2s^2 2p^4$ are calculated using the same plasma environmental potential belonging to the O^{1+} class. Even though the same environmental potential is used, the atomic potentials for individual electron configurations are all different, providing different energy levels and wave functions. By using the above averaging scheme, the simulation time becomes affordable, because the electronic structure calculations are performed on the number of visited electron configurations in different classes (∼100 in our case), rather than the number of individual atomic particles in the system (1050 in our simulation).

In addition, we eliminate the *ad hoc* muffin-tin-like approximation that had been employed [80], which imposed a constant connecting potential outside the touching radii of the atoms. In the current implementation, each atom class has its own asymptotic potential calculated up to a distance equal to half of the length of the shortest supercell edge. The ionization potential is evaluated with respect to this asymptotic value. We numerically confirmed that, for the dense aluminum case discussed in Ref. [80], the results obtained from the current framework and using the original muffin-tin approach show no significant difference. Moreover, the present choice has two advantages: On one hand, it improves the numerical convergence of the SCF procedure, in comparison with the muffin-tin-like approach employed in Ref. [80]. On the other hand, when there is no equilibrium, charges are not perfectly screened and therefore there may be transient potential gradients, which are captured by this approach (in contrast to the muffin-tin model).

We also note here that the SCF procedure may occasionally fail for an ion class for a given instantaneous environmental potential. In order to avoid the failure of the whole trajectory calculation in such cases, a set of fallback strategies was implemented in Ref. [80]. In essence, when there is an SCF failure, the environmental potential evaluated and used in an earlier time step is reused, thereby approximating the actual atomic parameters.

Note that XMDYN, in combination with XATOM, has been validated through comparison with a series of XFEL experiments (see Ref. [74] and references therein). More specifically, it successfully explained x-ray-induced nanoplasma formation in rare-gas clusters [44,45] and x-ray-driven fragmentation dynamics of gas-phase molecules [75,83–85]; it correctly captured the structural evolution of sulfur-sulfur pairs in a protein, as measured through SFX [23]; and it quantitatively reproduced the IPD observed in x-ray-heated aluminum [79,80].

III. RESULTS AND DISCUSSION

A. Simulation setup

We performed simulations on a bulk system of the simplest amino acid, glycine ($C_2H_5NO_2$), irradiated by an XFEL pulse with a photon energy of 10 keV and a pulse duration of 10 fs full width at half maximum (FWHM). Three photon fluences were considered: 1×10^{12}, 1×10^{13}, and 1×10^{14} ph/μm^2. The choices of the fluences were made on the basis of the delivering capability of current XFEL facilities. A uniform spatial irradiation throughout the sample was assumed. The bulk environment, mimicking the interior of biologically relevant macromolecules, is represented by simulating a supercell under periodic boundary conditions [76–78]. The simulation box contains 105 molecules and has dimensions of S_x=22.33 Å, S_y=21.95 Å, and S_z=19.68 Å. This setup corresponds to a mass density of 1.35 g/cm^3, which tallies with the typical protein density. In the limiting case of ionizing all 40 electrons from every single molecule in the simulation box, a maximum electron density of $\sim 4 \times 10^{23}$ cm^{-3} would be obtained, which is close to a typical solid density.

We used a time step of 0.5 as for time propagation and a soft-core radius of 0.6 a.u., i.e., the same values as used in Ref. [80], since the simulation results with those parameters quantitatively reproduced the IPDs that have been measured at an XFEL. When the transient IPD values were incorporated into the plasma dynamics simulations (i.e., when including IPD feedback), the plasma environmental potentials for individual atomic classes were evaluated in time steps of 100 as, in order to reduce the computational time, which is justified by the fact that the environmental potential varied smoothly on the femtosecond timescale in Ref. [80]. Still, XMDYN simulations with IPD feedback were much more expensive than those without IPD feedback. With the present setup of the simulation, we observed that the computational time including IPD feedback takes ∼3.5 times longer on average than that excluding IPD feedback.

To improve statistics, 150 XMDYN trajectories for each of the aforementioned fluences were calculated. The statistical error bars associated with the data underlying the figures in this paper are at most 2% of the range of the corresponding vertical-axis span. Therefore, the statistical error bars are not shown. SCF convergence issues arose in ∼1%−2% of the atomic parameter calculations and the fallback strategies [80] were used.

B. Plasma dynamics

Figure 1 illustrates plasma formation and evolution dynamics of the target system interacting with an XFEL pulse at a fluence of 1×10^{14} ph/μm^2. The peak of the XFEL pulse lies at t=14 fs and the system is propagated up to t=40 fs, as the temporal profile of the pulse is depicted with the shaded region in Fig. 1(c). Figure 1(a) shows an exemplary real-space snapshot of the target system at t=40 fs. The black, blue, red, and yellow balls represent C, N, O, and H species, respectively. The green dots indicate ionized electrons, forming a nonthermalized, solid-density plasma, as discussed in the following. The electron temperature is not yet well defined in this case because the electron kinetic energy distribution does not show any thermal equilibrium even at the end of the pulse, as illustrated in Fig. 1(b). In the energy range of 10–1000 eV, electrons were quasithermalized, but there is still a noticeable number of high-energy (∼10 keV) electrons out of equilibrium [86–88], which mainly came from photoionization.

In Fig. 1(c), we plot the time evolution of electron density and average kinetic energy of ionized electrons as an indicator of electron temperature. At the beginning, the average kinetic energy is high, i.e., starting from several keV. This is because, right after the first photoelectron ejections, there is still a negligible amount of slow free electrons (ejected in

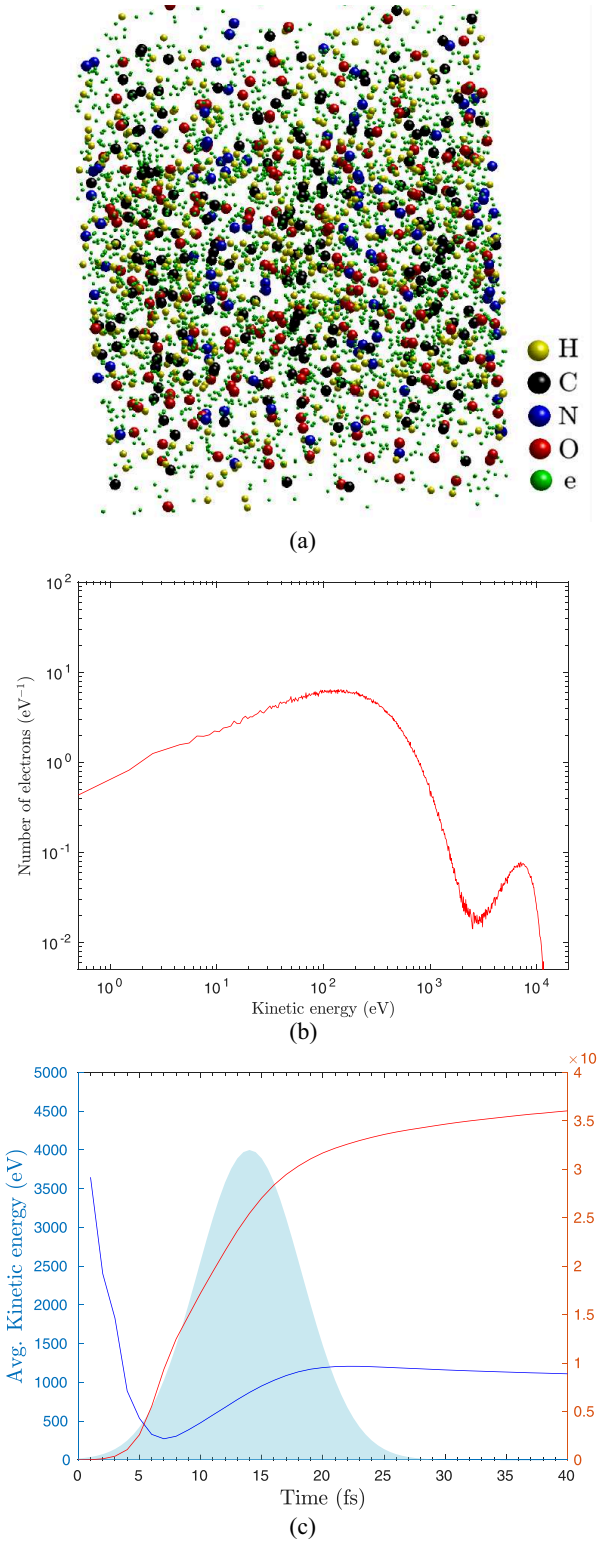

FIG. 1. Plasma formation dynamics of the glycine bulk system induced by an intense XFEL pulse with a fluence of 1×10^{14} ph/μm^2. (a) Real-space snapshot of the target system at $t = 40$ fs, i.e., after the interaction with the XFEL pulse. (b) Electron kinetic energy distribution at $t = 40$ fs. A varying bin width along the horizontal axis is used, which is 1% of the kinetic energy, but not smaller than 1 eV. (c) Time evolution of free electron density (red) and average electron kinetic energy (blue). The temporal pulse envelope is represented by the shaded region.

Auger-Meitner or collisional ionization events) beside the fast photoelectrons. However, the average kinetic energy drops within femtoseconds as such slow electrons appear at a high rate. As the pulse intensity increases, and, therefore, the photoionization rate as well, toward the center of the pulse, the increased energy absorption overall enhances the average free-electron kinetic energy up to ∼1 keV at the end of the simulation. The electron density reaches solid-state densities by the end of the pulse. Specifically, it comes close to $\sim 3.6 \times 10^{23}$ cm^{-3} in the demonstrated case.

Now, we turn to the analysis of how the electronic structure of individual atomic ions is influenced by a transient plasma environment evolving during the XFEL-matter interaction. In Fig. 2(a), as a representative example, the ionization potential (IP) values of oxygen $2p$, corresponding to the simulated realizations, are plotted as a function of time when the sample is interacting with an XFEL pulse at a fluence of 1×10^{13} ph/μm^2. In the left panel, the distinct lines show the IP values of isolated atomic ions. Different charge states are grouped with different colors, and multiple lines for the same charge state are due to various electron configurations. On the time-evolution panel, the transient IP values for each charge state are scattered over a broad energy range. This is, on one hand, because various electronic configurations belonging to the same charge state become populated. On the other hand, at any selected time, the transient plasma environment is different in different trajectories (=different realizations) due to the stochastic nature of the ionization processes, leading to dissimilar IPs. The characteristic splitting of the transient IPs is due to the differences between the no-core-hole (containing $1s^2$ occupation) and single-core-hole (containing $1s^1$ occupation) states. In the situation considered, double-core-hole states do not acquire a sufficiently high population to make a significant contribution. The differences between transient IPs and isolated-atom IPs for individual electron configurations provide transient IPD values.

In order to quantify how IPD depends on the atomic species and on the atomic charge state, time-integrated IPD values [79] of the $2p$ subshell are shown in Fig. 2(b) for C, N, and O species. Here, time-integrated IPD values were obtained after averaging over all realizations and all atomic particles for each class (atomic element and charge state) and over time (the error bars indicate the standard deviations). We numerically confirmed that these time-integrated IPD values are not significantly different for different subshells (similarly to Refs. [79,89]). However, they play different roles in the ionization dynamics. As an example, let us consider O^{2+} with a time-integrated IPD of ∼30 eV, as may be seen in Fig. 2(b). For $1s$ (isolated-atom IP ∼580 eV), the relative modification of the IP by the IPD effect is smaller than for $2s$ (isolated-atom IP ∼70 eV) and $2p$ (isolated-atom IP ∼50 eV). $1s$ ionization happens mainly through photoionization, while $2s$ and $2p$ ionizations are driven to a significant extent by collisional ionization. The relatively larger change in the valence IP also affects recombination processes. As collisional ionization in dense materials is the main mechanism for creating high charge states [41,42,53,76,80,90], the IPD effect potentially may affect the progression of the radiation damage.

One interesting observation in the time-integrated IPD values is that they are not very sensitive to the applied fluence.

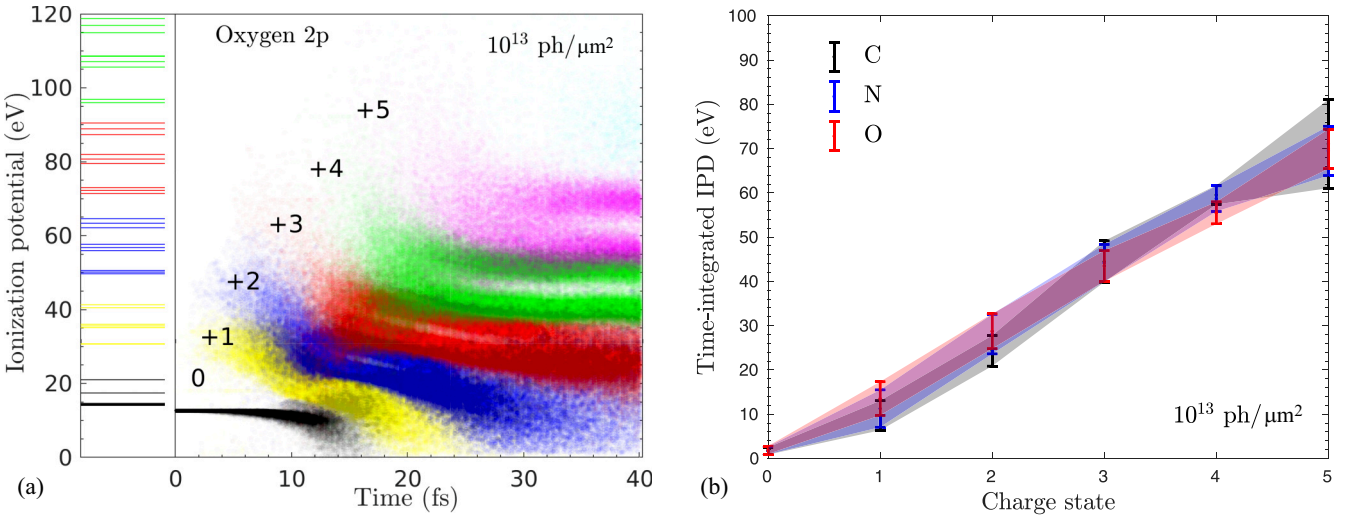

FIG. 2. (a) Transient IP values of $2p$ orbital in oxygen, obtained from all calculated realizations for different charge states at a fluence of 1×10^{13} ph/μm^2 . Horizontal lines at the left panel indicate IP values for the corresponding isolated atomic charges. Different colors represent different charge states. (b) Time-integrated IPD of $2p$ orbital for different charge states of each atomic species. Standard deviations are shown by the vertical error bars and the corresponding shaded region.

Figure 2(b) was obtained at a fluence of 1×10^{13} ph/μm^2 , but the absolute values for given charge states are similar for the other fluences we considered. Note that the fluence only determines the maximum charge state formed during ionization dynamics, whereas the time-integrated IPD values reflect the electron density at the time when a given charge state is most populated. Figure 3(a) shows the time evolution of the charge-state population of oxygen interacting with three different fluences. In Fig. 3(b), we plot the spatially averaged electron densities obtained at the time when the maximum population for each charge state is reached, for the three different fluence cases considered. The average electron densities at the maximum population of each charge state are similar to each other for different fluences, which explains the insensitivity of time-integrated IPD to the applied fluence. Thus, our results imply that the IPD values mainly depend on the given charge states, but not so much on the atomic species, different subshells, and x-ray fluence.

In Fig. 4, we examine the temporal evolution of the average molecular charge, representing the loss of the bound electrons. It is worthwhile to note that the degree of ionization here is drastically larger, in comparison with that of the isolated glycine molecule investigated in Ref. [91], because of plasma-induced processes included in the current study. For example, the average charge of an isolated glycine at a fluence of 1×10^{14} ph/μm^2 was not higher than +5 in the previous study [91], whereas it becomes higher than +30 for the bulk glycine. The particle density in the current study, which was chosen as a typical protein density, is sufficiently high to create a dense plasma and to induce significant enhancement

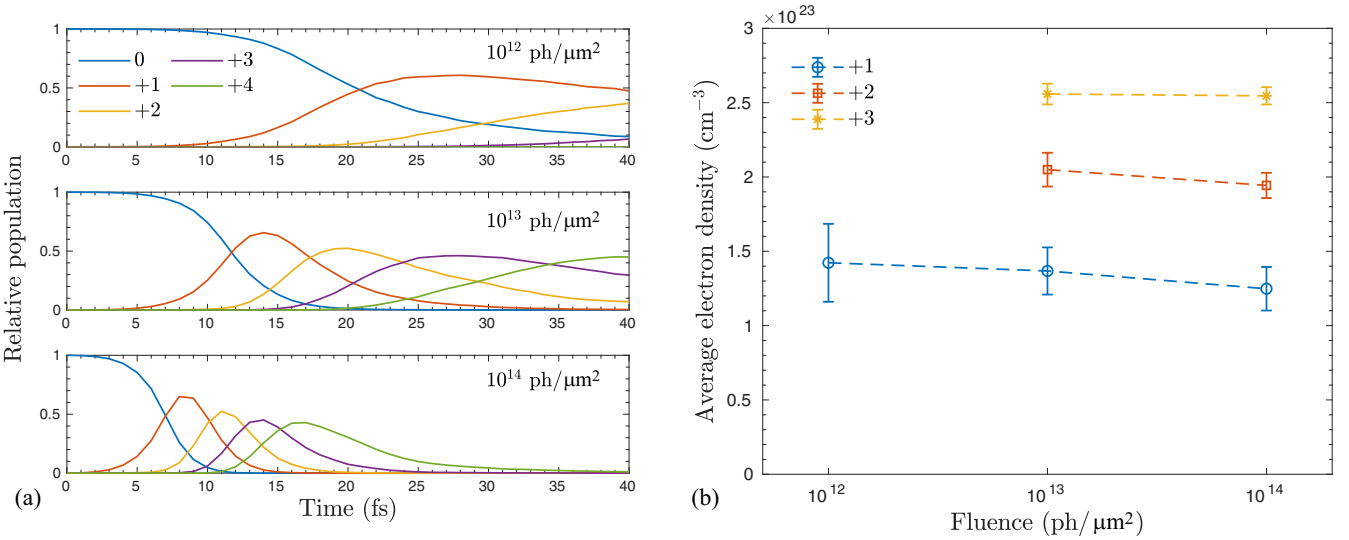

FIG. 3. (a) Time evolution of populations of various oxygen charge states, for three different fluences. (b) Average electron densities for different fluences corresponding to the situations where specific charge states have their peak population.

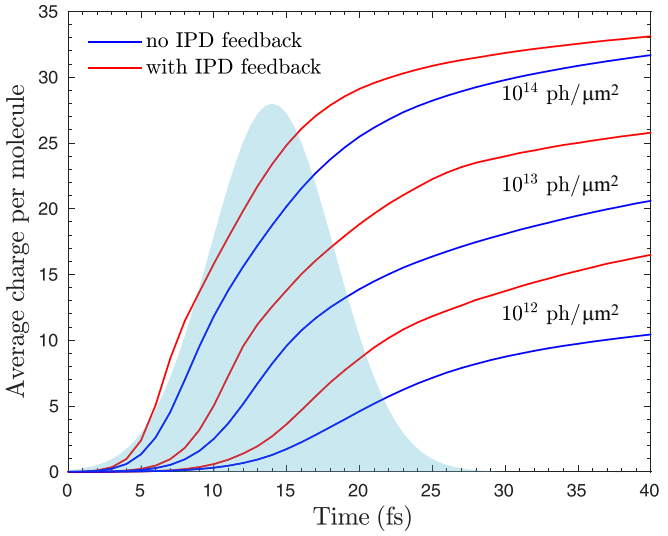

FIG. 4. Time evolution of average charge per glycine molecule at different fluences. The blue curve represents the result without IPD, whereas the red curve means that with IPD. The shaded region indicates the temporal Gaussian profile of the x-ray pulse considered in our simulations.

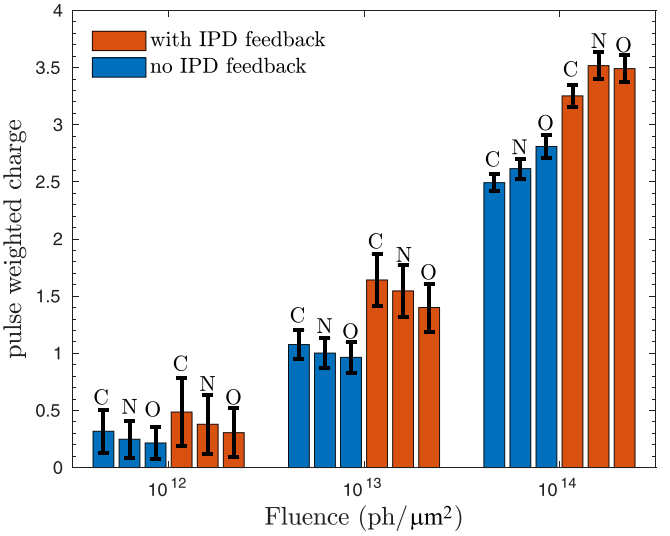

FIG. 5. Bar plot corresponds to the pulse-weighted average charge for nonhydrogen atoms at different fluences. The vertical error bars on the top show the standard deviation; they are not statistical errors, but they reflect how much in a given atom and a given x-ray pulse, the pulse-weighted charge should be expected to fluctuate about the mean. The red and blue bars represent the results with inclusion and exclusion of IPD, respectively.

in the degree of radiation damage due to collisional ionization. Figure 4 depicts the scenarios with exclusion (blue) and inclusion (red) of IPD feedback in the atomic electronic structure calculation during dynamics simulations. A certain increase in the average charge is observed due to inclusion of IPD feedback. For example, at a fluence of 1×10^{13} ph/μm^2 , there is a relative enhancement of the molecular charge by about 40% at the peak of the x-ray pulse. The increment becomes smaller as the fluence increases, particularly at the end of the pulse, due to the saturation of ionization.

C. Implications for SPI

In order to give more detailed insight into the overall degree of radiation damage affected by the plasma effects, we plot in Fig. 5 the pulse-weighted average charge for the individual atomic species, separately. The average charge for each atom is directly connected to the atomic form factor used in SPI because the form factor at vanishing photon momentum transfer ($Q = 0$) represents the number of electrons remaining bound to an atom during the x-ray pulse. Such a pulse-weighted, time-integrated measure is reasonable, since coherent scattering patterns are obtained as an incoherent sum of instantaneous patterns constructed with the atomic form factors weighted by the pulse intensity at every time point [78]. The blue color refers to the average charge without IPD and the red color to that with IPD. The differences between them indicate that inclusion of IPD in plasma modeling enhances the degree of ionization by 20%–40% for every atomic species in the sample for the given x-ray beam parameters. The pulse-weighted average atomic charge demonstrates that the difference with and without IPD increases on an absolute scale as the fluence increases, which is seemingly in contrast to the trend seen in the time-dependent plot in Fig. 4.

Another observation is that, for lower fluences, a heavier atom (C < N < O) is less ionized than a lighter one, because of a smaller collisional ionization cross section. At the highest fluence investigated, this behavior is reversed: A heavier atom gets more ionized because more electrons are available to be ionized.

The charge differences with and without IPD lie within a range of 0.1–1.0 per atom in absolute scale over the considered fluence regime, which is a significant effect. Moreover, as may be seen in Fig. 5, the impact of the IPD effect is somewhat higher or similar in the magnitude to the atomic-charge fluctuations that result from the stochastic nature of the ionization processes driving plasma formation. Advances in ultrahigh-resolution crystallography with sub-Å resolution may allow us to analyze charge densities of individual atoms [92,93]. Thus, in view of the results of our calculations, we would expect the IPD effect and quantum-mechanical charge-state fluctuations to become important once such a high spatial resolution can be achieved in SPI experiments.

The loss of the atomically bound electrons (indicated by the nonzero effective charges in Fig. 5) gives rise to overall fading of the scattering patterns. At the same time, considering that the number of bound electrons is the difference between the atomic number and the charge, one can also conclude, based on Fig. 5, that the contrast for distinguishing between different chemical elements in a reconstructed structure (i.e., the difference between the number of bound electrons for dissimilar elements) does not fade away, even when the IPD effect is included.

Besides the atomic (bound) electrons, the coherent scattering signal in SPI also strongly depends on the atomic positions. In our simulations, atomic positions are not fixed, but the displacements are practically negligible (<0.3 Å) at

the peak of the pulse, even at the highest fluence considered in this work. Thus, we do not expect that atomic movement causes significant changes to the coherent scattering signal.

IV. CONCLUSION

In the present study, we have investigated the radiation damage dynamics of bulk glycine during the interaction with a high-intensity ultrashort XFEL pulse at x-ray fluences that are practically relevant for SPI experiments. The analysis presented here anticipates how XFEL-generated plasma would influence the dynamics by modifying the binding energies of constituent atoms in typical biological macromolecules, such as proteins, under imaging conditions. Since our theoretical framework of XATOM and XMDYN is designed to handle compounds with arbitrary elemental composition, the present approach can be extended to high-Z-containing systems, such as metalloproteins.

We have shown that the XFEL-produced plasma does not attain thermodynamic equilibrium during the short pulse duration, and an NLTE treatment based on computing the real-time and real-space evolution of the system during the x-ray pulse is therefore appropriate to capture the transient modifications in electronic energy levels. Our work demonstrates an IPD ranging from a few electronvolts to tens of electronvolts, depending on the charge state of different atomic species. It is important to note that the present results for a biologically relevant model system reveal IPD values (up to $\sim$80 eV) that are similar in magnitude to those found in aluminum plasmas (up to $\sim$140 eV) and hence indicate the impact to be not much less than in a solid-density material. In comparison to valence binding energies and bond dissociation energies, this is a significant effect. Furthermore, we have shown that the average charge per molecule increases due to the inclusion of IPD feedback in each time step of the simulation. The pulse-weighted average charge for the nonhydrogen atoms demonstrates that the impact of IPD is quite strong for all fluences considered, revealing the influence of plasma-induced electronic-structure modifications on the atomic charge-state evolution during the x-ray pulse. The magnitude of this effect indicates the importance of the inclusion of IPD to appropriately capture fractional atomic charges in high-precision structure recovery. Nonetheless, as long as even approaching 1-Å resolution remains an open challenge in SPI, simulations excluding the IPD effect can provide a fair enough theoretical description at a comparatively low computational cost.

Finally, we note that so far, no IPD measurements have been performed in the context of SPI. Given the substantial impact of IPD suggested by our simulations, experimental validation on biologically relevant macromolecular systems is critical. Thus, we propose measuring IPD in biological samples via x-ray emission spectroscopy, as demonstrated for condensed-matter-density plasmas [51,52]. Our results indicate that the x-ray fluence determines the maximum charge state and that IPD strongly depends on the charge states formed during the ionization dynamics. In most cases in which XATOM and XMDYN were experimentally validated [44,45,75,83], the spatial distribution of the x-ray fluence in the interaction region with the target was quantitatively calibrated [94–96]. Without such a quantitative fluence calibration, it is impossible to determine through comparison with experimental data whether a given model is quantitatively predictive or not. To the best of our knowledge, such quantitative fluence calibrations have not yet been performed in connection with SFX and SPI experiments.

ACKNOWLEDGMENTS

S.B., Z.J., S.-K.S., and R.S. acknowledge support from DESY (Hamburg, Germany), a member of the Helmholtz Association HGF. R.S. further acknowledges support from the Cluster of Excellence "CUI: Advanced Imaging of Matter" of the Deutsche Forschungsgemeinschaft (DFG)-EXC 2056-project ID 390715994.

DATA AVAILABILITY

The data that support the findings of this article are not publicly available upon publication because it is not technically feasible and/or the cost of preparing, depositing, and hosting the data would be prohibitive within the terms of this research project. The data are available from the authors upon reasonable request.

[1] E. J. Milner-White, Protein three-dimensional structures at the origin of life, Interface Focus **9**, 20190057 (2019).
[2] E. F. Garman, Developments in x-ray crystallographic structure determination of biological macromolecules, Science **343**, 1102 (2014).
[3] E. P. Carpenter, K. Beis, A. D. Cameron, and S. Iwata, Overcoming the challenges of membrane protein crystallography, Curr. Opin. Struct. Biol. **18**, 581 (2008).
[4] S. Subramaniam and G. J. Kleywegt, A paradigm shift in structural biology, Nat. Methods **19**, 20 (2022).
[5] J. Jumper, *et al.*, Highly accurate protein structure prediction with AlphaFold, Nature (London) **596**, 583 (2021).
[6] L. M. Bertoline, A. N. Lima, J. E. Krieger, and S. K. Teixeira, Before and after AlphaFold2: An overview of protein structure prediction, Front. Bioinform. **3**, 1120370 (2023).
[7] J. Abramson, *et al.*, Accurate structure prediction of biomolecular interactions with AlphaFold 3, Nature (London) **630**, 493 (2024).
[8] Z. F. Brotzakis, S. Zhang, M. H. Murtada, and M. Vendruscolo, AlphaFold prediction of structural ensembles of disordered proteins, Nat. Commun. **16**, 1632 (2025).
[9] T. C. Terwilliger, D. Liebschner, T. I. Croll, C. J. Williams, A. J. McCoy, B. K. Poon, P. V. Afonine, R. D. Oeffner, J. S. Richardson, R. J. Read, and P. D. Adams, AlphaFold predictions are valuable hypotheses and accelerate but do not replace experimental structure determination, Nat. Methods **21**, 110 (2024).
[10] Y. Cheng, Single-particle Cryo-EM—How did it get here and where will it go, Science **361**, 876 (2018).
[11] Y. Cheng, Single-particle Cryo-EM at crystallographic resolution, Cell **161**, 450 (2015).

[12] M. Chen, M. F. Schmid, and W. Chiu, Improving resolution and resolvability of single-particle CryoEM structures using Gaussian mixture models, Nat. Methods **21**, 37 (2024).
[13] R. Neutze, R. Wouts, D. Van der Spoel, E. Weckert, and J. Hajdu, Potential for biomolecular imaging with femtosecond x-ray pulses, Nature (London) **406**, 752 (2000).
[14] M. J. Bogan, W. H. Benner, S. Boutet, U. Rohner, M. Frank, A. Barty, M. M. Seibert, F. Maia, S. Marchesini, S. Bajt, B. Woods, V. Riot, S. P. Hau-Riege, M. Svenda, E. Marklund, E. Spiller, J. Hajdu, and H. N. Chapman, Single particle x-ray diffractive imaging, Nano Lett. **8**, 310 (2008).
[15] M. Bergh, G. Huldt, N. Timneanu, F. R. Maia, and J. Hajdu, Feasibility of imaging living cells at subnanometer resolutions by ultrafast x-ray diffraction, Q. Rev. Biophys. **41**, 181 (2008).
[16] H. N. Chapman, *et al.*, Femtosecond x-ray protein nanocrystallography, Nature (London) **470**, 73 (2011).
[17] A. Barty, *et al.*, Self-terminating diffraction gates femtosecond x-ray nanocrystallography measurements, Nat. Photon. **6**, 35 (2012).
[18] P. Fromme and J. C. Spence, Femtosecond nanocrystallography using x-ray lasers for membrane protein structure determination, Curr. Opin. Struct. Biol. **21**, 509 (2011).
[19] T. R. M. Barends, L. Foucar, S. Botha, R. B. Doak, R. L. Shoeman, K. Nass, J. E. Koglin, G. J. Williams, S. Boutet, M. Messerschmidt, and I. Schlichting, *De novo* protein crystal structure determination from x-ray free-electron laser data, Nature (London) **505**, 244 (2014).
[20] S. Boutet, *et al.*, High-resolution protein structure determination by serial femtosecond crystallography, Science **337**, 362 (2012).
[21] H. N. Chapman, Serial femtosecond crystallography, Synchrotron Radiat. News **28**, 20 (2015).
[22] A. Aquila, *et al.*, Time-resolved protein nanocrystallography using an x-ray free-electron laser, Opt. Express **20**, 2706 (2012).
[23] K. Nass, *et al.*, Structural dynamics in proteins induced by and probed with x-ray free-electron laser pulses, Nat. Commun. **11**, 1814 (2020).
[24] G. Brändén and R. Neutze, Advances and challenges in time-resolved macromolecular crystallography, Science **373**, eaba0954 (2021).
[25] G. van der Schot, *et al.*, Imaging single cells in a beam of live cyanobacteria with an x-ray laser, Nat. Commun. **6**, 5704 (2015).
[26] M. F. Hantke, *et al.*, High-throughput imaging of heterogeneous cell organelles with an x-ray laser, Nat. Photon. **8**, 943 (2014).
[27] M. M. Seibert, *et al.*, Single mimivirus particles intercepted and imaged with an x-ray laser, Nature (London) **470**, 78 (2011).
[28] T. Ekeberg, *et al.*, Three-dimensional reconstruction of the giant mimivirus particle with an x-ray free-electron laser, Phys. Rev. Lett. **114**, 098102 (2015).
[29] A. Munke, *et al.*, Coherent diffraction of single rice dwarf virus particles using hard x-rays at the linac coherent light source, Sci. Data **3**, 160064 (2016).
[30] H. K. Reddy, *et al.*, Coherent soft x-ray diffraction imaging of coliphage PR772 at the linac coherent light source, Sci. Data **4**, 170079 (2017).
[31] H. N. Chapman, X-ray free-electron lasers for the structure and dynamics of macromolecules, Annu. Rev. Biochem. **88**, 35 (2019).
[32] J. Küpper, *et al.*, X-ray diffraction from isolated and strongly aligned gas-phase molecules with a free-electron laser, Phys. Rev. Lett. **112**, 083002 (2014).
[33] C. Fortmann-Grote, A. Buzmakov, Z. Jurek, N.-T. D. Loh, L. Samoylova, R. Santra, E. A. Schneidmiller, T. Tschentscher, S. Yakubov, C. H. Yoon, M. V. Yurkov, B. Ziaja-Motyka, and A. P. Mancuso, Start-to-end simulation of single-particle imaging using ultra-short pulses at the European X-ray Free-Electron Laser, IUCrJ **4**, 560 (2017).
[34] K. Ayyer, G. Geloni, V. Kocharyan, E. Saldin, S. Serkez, O. Yefanov, and I. Zagorodnov, Perspectives for imaging single protein molecules with the present design of the european XFEL, Struct. Dyn. **2**, 041702 (2015).
[35] K. Ayyer, A. J. Morgan, A. Aquila, H. DeMirci, B. G. Hogue, R. A. Kirian, P. L. Xavier, C. H. Yoon, H. N. Chapman, and A. Barty, Low-signal limit of x-ray single particle diffractive imaging, Opt. Express **27**, 37816 (2019).
[36] K. Ayyer, *et al.*, 3D diffractive imaging of nanoparticle ensembles using an x-ray laser, Optica **8**, 15 (2021).
[37] I. V. Lundholm, *et al.*, Considerations for three-dimensional image reconstruction from experimental data in coherent diffractive imaging, IUCrJ **5**, 531 (2018).
[38] E. Sobolev, *et al.*, Megahertz single-particle imaging at the European XFEL, Commun. Phys. **3**, 97 (2020).
[39] S. P. Hau-Riege, R. A. London, and A. Szoke, Dynamics of biological molecules irradiated by short x-ray pulses, Phys. Rev. E **69**, 051906 (2004).
[40] L. Lomb, *et al.*, Radiation damage in protein serial femtosecond crystallography using an x-ray free-electron laser, Phys. Rev. B **84**, 214111 (2011).
[41] S. M. Vinko, *et al.*, Creation and diagnosis of a solid-density plasma with an x-ray free-electron laser, Nature (London) **482**, 59 (2012).
[42] S. M. Vinko, *et al.*, Investigation of femtosecond collisional ionization rates in a solid-density aluminium plasma, Nat. Commun. **6**, 6397 (2015).
[43] T. Gorkhover, *et al.*, Nanoplasma dynamics of single large xenon clusters irradiated with superintense x-ray pulses from the linac coherent light source free-electron laser, Phys. Rev. Lett. **108**, 245005 (2012).
[44] T. Tachibana, *et al.*, Nanoplasma formation by high intensity hard x-rays, Sci. Rep. **5**, 10977 (2015).
[45] Y. Kumagai, *et al.*, Radiation-induced chemical dynamics in ar clusters exposed to strong x-ray pulses, Phys. Rev. Lett. **120**, 223201 (2018).
[46] C. Caleman, G. Huldt, F. R. Maia, C. Ortiz, F. G. Parak, J. Hajdu, D. van der Spoel, H. N. Chapman, and N. Timneanu, On the feasibility of nanocrystal imaging using intense and ultrashort x-ray pulses, ACS Nano **5**, 139 (2011).
[47] H. O. Jönsson, N. Tîmneanu, C. Östlin, H. A. Scott, and C. Caleman, Simulations of radiation damage as a function of the temporal pulse profile in femtosecond x-ray protein crystallography, J. Synchrotron Rad. **22**, 256 (2015).
[48] G. Ecker and W. Kröll, Lowering of the ionization energy for a plasma in thermodynamic equilibrium, Phys. Fluids **6**, 62 (1963).
[49] J. C. Stewart and K. D. Pyatt Jr, Lowering of ionization potentials in plasmas, Astrophys. J. **144**, 1203 (1966).

[50] B. I. Cho, *et al.*, Resonant $K\alpha$ spectroscopy of solid-density aluminum plasmas, Phys. Rev. Lett. **109**, 245003 (2012).

[51] O. Ciricosta, *et al.*, Direct measurements of the ionization potential depression in a dense plasma, Phys. Rev. Lett. **109**, 065002 (2012).

[52] O. Ciricosta, *et al.*, Measurements of continuum lowering in solid-density plasmas created from elements and compounds, Nat. Commun. **7**, 11713 (2016).

[53] Q. Y. van den Berg, E. V. Fernandez-Tello, T. Burian, J. Chalupský, H.-K. Chung, O. Ciricosta, G. L. Dakovski, V. Hájková, P. Hollebon, L. Juha, J. Krzywinski, R. W. Lee, M. P. Minitti, T. R. Preston, A. G. de la Varga, V. Vozda, U. Zastrau, J. S. Wark, P. Velarde, and S. M. Vinko, Clocking femtosecond collisional dynamics via resonant x-ray spectroscopy, Phys. Rev. Lett. **120**, 055002 (2018).

[54] J. Zeng, C. Ye, Y. Li, and J. Yuan, Ionization potential depression in dense iron plasmas near solid density, Results Phys. **40**, 105836 (2022).

[55] L. Mercadier, *et al.*, Transient absorption of warm dense matter created by an x-ray free-electron laser, Nat. Phys. **20**, 1564 (2024).

[56] I. Dawod, S. Cardoch, T. André, E. De Santis, A. P. Mancuso, C. Caleman, and N. Timneanu, Moldstruct: Modeling the dynamics and structure of matter exposed to ultrafast x-ray lasers with hybrid collisional-radiative/molecular dynamics, J. Chem. Phys. **160**, 184112 (2024).

[57] R. Thiele, S.-K. Son, B. Ziaja, and R. Santra, Effect of screening by external charges on the atomic orbitals and photoinduced processes within the Hartree-Fock-Slater atom, Phys. Rev. A **86**, 033411 (2012).

[58] J. Bauche, C. Bauche-Arnoult, and O. Peyrusse, *Atomic Properties in Hot Plasmas: From Levels to Superconfigurations* (Springer, Cham, 2015).

[59] D. Agassi, Phenomenological model for pisosecond-pulse laser annealing of semiconductors, J. Appl. Phys. **55**, 4376 (1984).

[60] P. L. Silvestrelli, A. Alavi, M. Parrinello, and D. Frenkel, *Ab initio* molecular dynamics simulation of laser melting of silicon, Phys. Rev. Lett. **77**, 3149 (1996).

[61] K. K. Ostrikov, F. Beg, and A. Ng, *Colloquium:* Nanoplasmas generated by intense radiation, Rev. Mod. Phys. **88**, 011001 (2016).

[62] N. Medvedev, U. Zastrau, E. Förster, D. O. Gericke, and B. Rethfeld, Short-time electron dynamics in aluminum excited by femtosecond extreme ultraviolet radiation, Phys. Rev. Lett. **107**, 165003 (2011).

[63] B. Ziaja, Z. Jurek, N. Medvedev, V. Saxena, S.-K. Son, and R. Santra, Towards realistic simulations of macromolecules irradiated under the conditions of coherent diffraction imaging with an x-ray free-electron laser, Photonics **2**, 256 (2015).

[64] *Modern Methods in Collisional-Radiative Modeling of Plasmas*, 1st ed., edited by Y. Ralchenko (Springer, Cham, 2016).

[65] J. J. Bekx, S.-K. Son, B. Ziaja, and R. Santra, Electronic-structure calculations for nonisothermal warm dense matter, Phys. Rev. Res. **2**, 033061 (2020).

[66] S. Anisimov, B. Kapeliovich, and T. Perel'man, Electron emission from metal surfaces exposed to ultrashort laser pulses, Sov. Phys. JETP **39**, 375 (1974).

[67] B. Rethfeld, D. S. Ivanov, M. E. Garcia, and S. I. Anisimov, Modelling ultrafast laser ablation, J. Phys. D: Appl. Phys. **50**, 193001 (2017).

[68] H. A. Scott, CRETIN—A radiative transfer capability for laboratory plasmas, J. Quant. Spectrosc. Radiat. Transfer **71**, 689 (2001).

[69] H.-K. Chung, M. Chen, W. Morgan, Y. Ralchenko, and R. Lee, FLYCHK: Generalized population kinetics and spectral model for rapid spectroscopic analysis for all elements, High Energy Density Phys. **1**, 3 (2005).

[70] S. B. Hansen, H.-K. Chung, C. J. Fontes, Y. Ralchenko, H. Scott, and E. Stambulchik, Review of the 10th non-LTE code comparison workshop, High Energy Density Phys. **35**, 100693 (2020).

[71] X. Han, L. Li, Z. Dai, and W. Zheng, MAICRM: A general model for rapid simulation of hot dense plasma spectra, High Energy Density Phys. **39**, 100943 (2021).

[72] B. Deschaud, O. Peyrusse, and F. Rosmej, Simulation of XFEL induced fluorescence spectra of hollow ions and studies of dense plasma effects, Phys. Plasmas **27**, 063303 (2020).

[73] D. R. Bates, A. E. Kingston, and R. W. P. McWhirter, Recombination between electrons and atomic ions, I. Optically thin plasmas, Proc. R. Soc. London A **267**, 297 (1962).

[74] Z. Jurek, S.-K. Son, B. Ziaja, and R. Santra, XMDYN and XATOM: Versatile simulation tools for quantitative modeling of x-ray free-electron laser induced dynamics of matter, J. Appl. Crystallogr. **49**, 1048 (2016).

[75] B. F. Murphy, *et al.*, Femtosecond x-ray-induced explosion of C_{60} at extreme intensity, Nat. Commun. **5**, 4281 (2014).

[76] M. M. Abdullah, Z. Jurek, S.-K. Son, and R. Santra, Calculation of x-ray scattering patterns from nanocrystals at high x-ray intensity, Struct. Dyn. **3**, 054101 (2016).

[77] M. M. Abdullah, Anurag, Z. Jurek, S.-K. Son, and R. Santra, Molecular-dynamics approach for studying the nonequilibrium behavior of x-ray-heated solid-density matter, Phys. Rev. E **96**, 023205 (2017).

[78] M. M. Abdullah, S.-K. Son, Z. Jurek, and R. Santra, Towards the theoretical limitations of x-ray nanocrystallography at high intensity: The validity of the effective-form-factor description, IUCrJ **5**, 699 (2018).

[79] R. Jin, M. M. Abdullah, Z. Jurek, R. Santra, and S.-K. Son, Transient ionization potential depression in nonthermal dense plasmas at high x-ray intensity, Phys. Rev. E **103**, 023203 (2021).

[80] R. Jin, Z. Jurek, R. Santra, and S.-K. Son, Plasma environmental effects in the atomic structure for simulating x-ray free-electron-laser-heated solid-density matter, Phys. Rev. E **106**, 015206 (2022).

[81] L. Inhester, Z. Jurek, S.-K. Son, M. M. Abdullah, and R. Santra, XRAYPAC—A software package for modeling x-ray-induced dynamics of matter, version 2.1.0, GitLab (2025), https://gitlab.desy.de/CDT/xraypac.

[82] S.-K. Son, L. Young, and R. Santra, Impact of hollow-atom formation on coherent x-ray scattering at high intensity, Phys. Rev. A **83**, 033402 (2011).

[83] N. Berrah, *et al.*, Femtosecond-resolved observation of the fragmentation of buckminsterfullerene following x-ray multiphoton ionization, Nat. Phys. **15**, 1279 (2019).

[84] R. Boll, *et al.*, X-ray multiphoton-induced Coulomb explosion images complex single molecules, Nat. Phys. **18**, 423 (2022).

[85] B. Richard, *et al.*, Imaging collective quantum fluctuations of the structure of a complex molecule, Science **389**, 650 (2025).

[86] S. P. Hau-Riege, Nonequilibrium electron dynamics in materials driven by high-intensity x-ray pulses, Phys. Rev. E **87**, 053102 (2013).

[87] M. Šmíd, O. Renner, A. Colaitis, V. T. Tikhonchuk, T. Schlegel, and F. B. Rosmej, Characterization of suprathermal electrons inside a laser accelerated plasma via highly-resolved Kα-emission, Nat. Commun. **10**, 4212 (2019).

[88] S. Ren, Y. Shi, Q. Y. van den Berg, M. F. Kasim, H.-K. Chung, E. V. Fernandez-Tello, P. Velarde, J. S. Wark, and S. M. Vinko, Non-thermal evolution of dense plasmas driven by intense x-ray fields, Commun. Phys. **6**, 99 (2023).

[89] S.-K. Son, R. Thiele, Z. Jurek, B. Ziaja, and R. Santra, Quantum mechanical calculation of ionization-potential lowering in dense plasmas, Phys. Rev. X **4**, 031004 (2014).

[90] B. Ziaja, R. A. London, and J. Hajdu, Unified model of secondary electron cascades in diamond, J. Appl. Phys. **97**, 064905 (2005).

[91] S. Banerjee, Z. Jurek, M. M. Abdullah, and R. Santra, Chemical effects on the dynamics of organic molecules irradiated with high intensity x rays, Struct. Dyn. **9**, 054101 (2022).

[92] C. Jelsch, M. M. Teeter, V. Lamzin, V. Pichon-Pesme, R. H. Blessing, and C. Lecomte, Accurate protein crystallography at ultra-high resolution: Valence electron distribution in crambin, Proc. Natl. Acad. Sci. USA **97**, 3171 (2000).

[93] J. C.-H. Chen, M. Gilski, C. Chang, D. Borek, G. Rosenbaum, A. Lavens, Z. Otwinowski, M. Kubicki, Z. Dauter, M. Jaskolski, and A. Joachimiak, Solvent organization in the ultrahigh-resolution crystal structure of crambin at room temperature, IUCrJ **11**, 649 (2024).

[94] K. Toyota, Z. Jurek, S.-K. Son, H. Fukuzawa, K. Ueda, N. Berrah, B. Rudek, D. Rolles, A. Rudenko, and R. Santra, *xcalib*: A focal spot calibrator for intense x-ray free-electron laser pulses based on the charge state distributions of light atoms, J. Synchrotron Radiat. **26**, 1017 (2019).

[95] N. Breckwoldt, S.-K. Son, T. Mazza, A. Rörig, R. Boll, M. Meyer, A. C. LaForge, D. Mishra, N. Berrah, and R. Santra, Machine-learning calibration of intense x-ray free-electron-laser pulses using Bayesian optimization, Phys. Rev. Res. **5**, 023114 (2023).

[96] T. Mazza, *et al.*, The beam transport system for the small quantum systems instrument at the European XFEL: Optical layout and first commissioning results, J. Synchrotron Radiat. **30**, 457 (2023).